Depth from Defocus Technique for High Number Density Particle Images

Rixin Xu[1, 2], Zuojie Huang[1, 2], Wenchao Gong[1, 2], Wu Zhou[1, 2,*], Cameron Tropea[3,*]

1: School of Energy and Power Engineering, University of Shanghai for Science and Technology, Shanghai, China
2: Shanghai Key Laboratory of Multiphase Flow and Heat Transfer for Power Engineering, University of Shanghai for Science and Technology, Shanghai, China
3: Institute for Fluid Mechanics and Aerodynamics, Technical University of Darmstadt, Darmstadt , Germany
*Corresponding author: zhouwu@usst.edu.cn, tropea@sla.tu-darmstadt.de

Keywords: two-phase flow, particle sizing, irregular, High Particle Concentrations, Convolutional Neural Networks.

ABSTRACT

The Depth from Defocus (DFD) imaging technique is used to measure the size and number concentration of particles in dispersed two-phase flows, but until now it has primarily been applied to low concentration particle images. This study explores how the technique can be extended to handle overlapping images caused by neighboring particles, significantly broadening the application scope of the DFD technique and enabling measurements at higher particle number/volume concentrations. The processing algorithms are experimentally validated using a dedicated apparatus that can systematically vary particle size, shape, and degree of image overlap. Additionally, this study explores the use of Convolutional Neural Networks (CNN) for this task, comparing these results with those obtained using conventional analyses in terms of accuracy, tolerable concentration limits, and computational speed. This approach requires a large teaching dataset of images, which is only practical and feasible if the dataset can be synthetically generated. An image generation procedure for out-of-focus neighboring spherical particles, resulting in a known blurred image overlap, is therefore first developed. This procedure is validated using laboratory images with known particle size distribution, position, and image overlap before creating the teaching dataset. The trained processing scheme is then applied to both synthetic datasets and experimental data, allowing the evaluation of the technique's limits in terms of image overlap and tolerable volume concentration, as a function of particle size distribution.

1. Introduction

The technique of obtaining depth and size information from defocused blurry images of particles is known as Depth from Defocus (DFD). This concept was initially proposed in Pentland (1987) and has since become one of the popular depth estimation techniques, parallel to stereo vision and holographic imaging. This method can be used to determine the size and location of spherical particles in a fluid, even when their position is beyond the depth of field limit; thus, out of focus. Moreover, this allows all particles within a well-defined volume to be counted and sized, allowing accurate measurement of number and volume concentration.

The DFD principle can be implemented through various optical means to obtain defocused images, including changing aperture between two exposures, thus inducing a controlled defocus in the formed images. Alternatively, the technique has been realized using either one or two cameras. In both cases the goal is to identify and size particles over a three-dimensional volume, while also determining their coordinates. With appropriately fast cameras, it is possible to resolve the trajectory of the particles in time using particle tracking velocimetry (Willert & Gharib, 1992; Murata & Kawamura, 1999; Bao & Li, 2011), although this aspect will not be elaborated further in the present study.

First defocus systems for particle measurement used two images, varying the defocus blur by adjusting imaging system parameters between images, such as aperture, focal length, and the distance from the lens to the camera imaging plane (Subbarao & Gurumoorthy, 1988; Surya & Subbarao, 1993). In the study by Lebrun et al. (1994), a beam splitter was employed to evenly divide the imaging rays into two cameras. By adjusting the spacers connecting the dual camera setup, it became possible to simultaneously capture two images of particles with different degrees of blur at a specific moment, with one camera. The disparity in blur between these two images was used to assess defocus ambiguity. In terms of image processing, various methods were employed in the early stages, including spatial domain deconvolution restoration (Ens & Lawrence, 1991) and frequency domain processing, using a Fourier transformation (Zhou, Luo, et al., 2020), to identify the degree of blur in particle images, corresponding to their depth position. More recent work involving two cameras employed a single normalized gray level threshold and two calibrated size-independent relations to measure size and depth location (Zhou, Tropea, et al., 2020). The sensitivity of this technique to a large number of optical and system realization parameters has been investigated in Zhou et al. (2021) and has been used for shock-drop interaction studies in Sharma et al. (2023).

More attractive in terms of equipment complexity is the one camera realization, realized in a number of configurations in the past (Subbarao, 1988; Cierpka et al., 2010). One particular configuration uses a cylindrical lens in the imaging optics, such that the out-of-focus condition results in an astigmatism to determine the position of the particle along the optical axis (Barnkob et al., 2015; Barnkob & Rossi, 2020). Recently, neural networks have been adopted to deal with these out-of-focus images (Barnkob et al., 2021; Zhang et al., 2023). In addition, there is a method for particle depth position measurement by employing specially shaped aperture configurations, primarily including three-hole apertures and annular apertures (Willert & Gharib, 1992; Pereira & Gharib, 2002; Levin et al., 2007). The arrangements of these apertures allow for determining whether particle coordinates are in front of or behind the object plane. On the other hand, the emphasis of these studies has not been placed on also determining the size of the particles. Jatin Rao et al. (2024) used a novel theoretical calibration method to obtain the relationship between gray level gradient and blur kernel size. This theoretical analysis method was employed by Xu et al. (2024) to analyze overlapping particle images.

Recently, numerous studies have applied deep learning techniques to measure out-of-focus particles. Wang et al. (2022a) examined the sizing of out-of-focus spherical particles using a deep-learning method, which was extended to location measurement (Wang et al. (2022b)). However, the present study focuses on determining the size and position of spherical particles in a two-phase flow where particle images overlap, with primary blurring caused by out-of-focus blurring. Sachs et al. (2023) and Ratz et al. (2023) utilized deep neural networks (DNN) for depth and position measurement of seeding particles in microchannels, and Zhang et al. (2023) used deep learning and generative adversarial networks (GAN) to detect particle depth positions and deblurring from defocused images.

2. Measurement Principle

2.1. Analytic Relations for a Single Camera DFD

This description will intentionally be kept brief, because it simply summarizes the work in Jatin Rao et al. (2024). Typical images from in-focus and out-of-focus particles are illustrated in Fig. 1. From this figure, it is evident that the degree of image blur depends on the out-of-focus distance z from the object plane. However, also the gradient of the gray level changes with z. These blurred images can be described by a convolution of the focused image $f(x, y)$ of a particle with a blur kernel $h(x, y)$ (Blaisot & Yon, 2005; Zhou, Tropea, et al., 2020). The intensity g_t at any location on the sensor plane (x, y) is then evaluated as:

$$g_\mathrm{t}(x, y) = f(x, y) \circledast h(x, y) \tag{1}$$

where $f(x, y)$ is a normalized intensity of the in-focus particle on the image plane

$$\begin{aligned} f(x, y) &= 0, \text{ if outside particle contour} \\ &= 1, \text{ if inside particle contour} \end{aligned} \tag{2}$$

The particle dimensions on the image plane are related to the actual size through the magnification factor of the optical system, M. The blur kernel $h(x, y)$ can be approximated by a Gaussian function with σ as the standard deviation (Junjie et al., 2023):

$$h(x, y) = \frac{1}{2\pi\sigma^2} e^{-\frac{x^2+y^2}{2\sigma^2}} \tag{3}$$

This assumes that the point spread function has a central peak much narrower in width than σ, which is fulfilled in typical DFD optical systems (Jatin Rao et al., 2024). The standard deviation σ represents the degree of blur or size of the blur kernel and is proportional to the displacement of the particle away from the object plane (Δz),

$$\sigma = \beta |z| \tag{4}$$

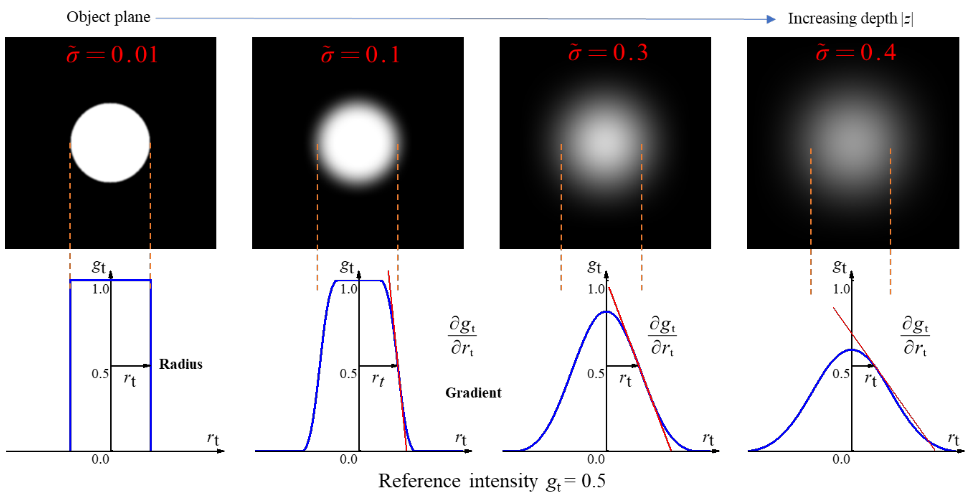

Figure 1. Illustration of particle image and resulting intensity distribution for varying degrees of out-of-focus. Two quantities are extracted from the images – radius (r_t) and intensity gradient ($\partial g_t / \partial r_t$) at a reference intensity value (g_t=0.5), both of which decrease with increasing depth from the object plane. $\tilde{\sigma}$ is a dimensionless σ defined in Eq. (5).

where β describes the proportionality and is constant for a given optical system. Furthermore, we assume that telecentric lenses are used on both the illumination and receiving sides of the optical system; hence, the magnification does not change with particle z position.

Given this description of the blurred images, there are several avenues to follow with the aim of determining the original image from the defocussed blurred image $g_t(x, y)$. Conventional approaches use a non-blind deconvolution. This is non-blind since the blur kernel is known, arising from Gaussian defocus blurring and the point spread function (which in practical systems is negligibly small). The most common non-blind deblurring methods employ the Wiener filter (Wiener (1949)) or the Richardson-Lucy algorithm (Richardson (1972)). More recently, the performance of these conventional approaches has been significantly enhanced by integrating them with learned deep features (Dong et al. (2021)). Although these approaches are capable of reconstructing the high resolution, deblurred images, the location of the particle on the z axis is not available. For this reason, a different approach is used in the present study in that the convolution integral is explicitly solved for spherical particles. Having this, and a quantitative calibration of the parameter β, the particle z position can be found.

For spherical particles the convolution integral can be solved and using the following dimensionless variables

$$\widetilde{\rho} = \frac{r}{d_o}, \quad \widetilde{\rho}_t = \frac{r_t}{d_o}, \quad \widetilde{\sigma} = \frac{\sigma}{d_o} \tag{5}$$

the integral can be expressed in dimensionless form as

$$g_t\left(\widetilde{\rho}_t\right) = \frac{1}{\widetilde{\sigma}^2} \int_0^{1/2} e^{-\frac{\widetilde{\rho}^2 + \widetilde{\rho}_t^2}{2\widetilde{\sigma}^2}} I_o\left(\frac{\widetilde{\rho}\widetilde{\rho}_t}{\widetilde{\sigma}^2}\right) \widetilde{\rho} d\widetilde{\rho} \tag{6}$$

where I_o is the zeroth order modified Bessel function of the first kind and d_0 is the true particle diameter (Rao, Sharma, Basu, & Tropea, 2024).

From the particle image, two quantities are extracted – the radius (r_t) and intensity gradient $(\partial g_\mathrm{t}/\partial r_\mathrm{t})$ at a reference intensity value, e.g., $g_\mathrm{t} = 0.5$. Both of these quantities decrease as the particle is further displaced from the object plane ($z = 0$) (Fig. 1). This suggests that the gray level gradient can be used to estimate the parameter σ in the blur kernel. In Jatin Rao et al. (2024) a novel measurable dimensionless radius is proposed (Rao, Sharma, Tropea, & Basu, 2024):

$$\widetilde{R}_\mathrm{t} = \left(\frac{\widetilde{\rho}_\mathrm{t}}{(\widetilde{\rho}_\mathrm{t})_{g_\mathrm{t}=0.5}}\right)_{\widetilde{\sigma}} = \left(\frac{r_\mathrm{t}}{(r_\mathrm{t})_{g_\mathrm{t}=0.5}}\right)_{\widetilde{\sigma}} \tag{7}$$

where $(r_\mathrm{t})_{g_\mathrm{t}=0.5}$ is the radius at the reference intensity. The proposed functional form of the analytic function is

$$\widetilde{G} = \left|\frac{\partial g_\mathrm{t}}{\partial \widetilde{R}_\mathrm{t}}\right|_{g_\mathrm{t}=0.5} = \left|r_\mathrm{t}\frac{\partial g_\mathrm{t}}{\partial r_\mathrm{t}}\right|_{g_\mathrm{t}=0.5} = f_2\left(\widetilde{\sigma}\right) \tag{8}$$

From this dimensionless version of intensity gradient $|\partial g_\mathrm{t}/\partial \widetilde{R}_\mathrm{t}| = |r_\mathrm{t}\partial g_\mathrm{t}/\partial r_\mathrm{t}|$ at the reference intensity (subscript $g_\mathrm{t} = 0.5$ is omitted from now on), we can estimate the dimensionless depth, expressed as a dimensionless standard deviation of the blurring $\widetilde{\sigma}$. Note that in Jatin Rao et al. (2024), a limiting value of $\widetilde{\sigma} = 0.35$ was recommended, below which the size measurement would be reliable.

Another function is necessary to estimate $\widetilde{\rho}_\mathrm{t}$ from $\widetilde{\sigma}$ at the reference intensity, represented in the functional form as

$$\widetilde{\rho}_\mathrm{t} = f_1(\widetilde{\sigma}) \tag{9}$$

These functions can be further combined in the form $\widetilde{\rho}_\mathrm{t} = f_1(f_2^{-1}(\widetilde{G}))$. So the particle diameter d_o can be measured after obtaining $\widetilde{G}$ and r_t from the particle image.

The calibration is necessary not for the size determination, but for the position, i.e., β in Eq. (4). This calibration consists of moving a reticle target along the z axis while registering the standard deviation σ, using the function $\widetilde{\sigma} = f_2^{-1}(\widetilde{G})$ and the true particle diameter d_o.

2.2. Analysis using Convolutional Neural Networks

Training deep learning models typically requires large datasets, which implies a significant amount of manual annotation. In some commonly used segmentation scenarios for Mask R-CNN, the objects to be segmented have clear edges, and datasets for such objects can be annotated using auxiliary annotation tools. However, for this application, the edges of the captured out-of-focus particle images are difficult for the human eye to discern, making it challenging to accurately delineate them manually or obtain large training data through more automated methods. Therefore, in the present study out-of-focus particle images are simulated using the degradation function models of single particles and overlapping particles mentioned in the previous section, as the dataset input for network training. Gaussian blur convolution with different standard deviations is used to simulate particles in images with varying degrees of out-of-focus blurring (z positions). For overlapping particles, in addition to generating different degrees of blurring, different orientations and overlap ratios (OLR) (Xu et al. (2024)) are also generated.

Considering that different light intensities, sensitivities of image sensors, and transmittance of media to particles will affect the grayscale of particles and background in images, random values are set for the background gray level and particle gray level to ensure that the gray level is uniformly distributed within a certain range. The pixel diameter of particles is set to a random integer in the range of 5 to 400, the gray level of particles is a random integer in the range of 0 to 50, and the gray level of the background is a random integer in the range of 100 to 255. Note that the image is assumed to have an 8 bit resolution in gray level. Since there is an upper limit to the performance of the model, such as when the blurring of particles is very high and the gray level difference between particles and background is very small, the model may have difficulty learning features, which may lead to a decrease in the accuracy of the trained model. Therefore, an upper limit on blurring degree is set in the training set.

When using the same Gaussian blur kernel, images of smaller particles have lower contrast with the background compared to larger particles. Thus, under the same blurring degree, the feature information of smaller particles is less obvious compared to larger particles. Therefore, different blur limits are set for particles of different sizes. In the present study, the blur limit of each particle is set as $\tilde{\sigma} = \sigma/d_0 = 0.35$, as in Jatin Rao et al. (2024), based on the ratio of blur kernel standard deviation to the pixel diameter of the particle, d_0. Additionally, to prevent overfitting, Gaussian noise with a standard deviation of 0.01% is added.

The resolution of each image generated in the training set is 480 px $\times$ 480 px, with each image corresponding to one out-of-focus particle. A total of 51,735 images including different levels of defocus, different background gray levels, different particle gray levels, and different particle sizes, were generated; 63,140 images of overlapping particles with different levels of defocus, sizes, and overlapping orientations were generated. Typical training images are shown in Fig. 2.

The hardware configuration of the training platform consists of an Intel(R) Xeon(R) Silver 4210R CPU@2.40GHz CPU and an NVIDIA GeForce RTX 2080Ti 11G graphics card. The aforementioned training set and corresponding labels are input into the network, and training is conducted based on the pre-trained weights of the MS COCO (Lin et al. (2014)) dataset, which accelerates the convergence speed and reduces the training time, as shown in the training process flow chart of Fig. 3.

Three scales of learning rates were attempted: 0.01, 0.001, and 0.0001. It was found that when

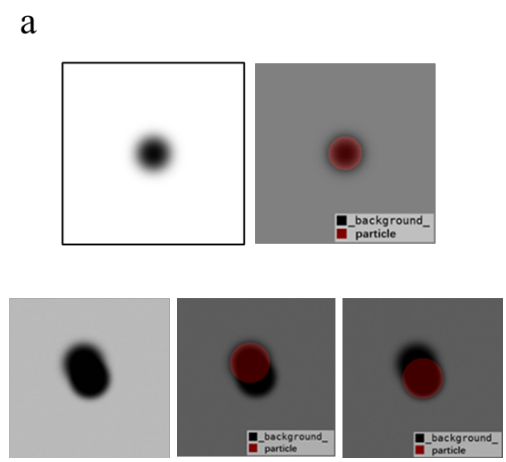

Figure 2. Typical training images:(a) Single particle original image and mask image; (b) Overlapping particles original image and mask image.

the learning rate was set to 0.01, the training loss decreased slowly, while when set to 0.0001, the loss function was difficult to reduce after reaching a certain level, suggesting that the learning rate may be too low, leading to convergence to a local optimum. Finally, 0.001 was selected as the learning rate for model training. According to the loss function curve, the overall network loss initially decreases rapidly, followed by a gradual decrease, tending to converge. After 200 rounds of training, the network loss stabilizes at around 0.03, indicating that the network has been trained well at this point. The entire training process took 25 hours.

3. Image Processing Algorithms

3.1. Procedure for Spherical Particles with Overlapping Images

We begin by reviewing the procedure for circular images arising from non-overlapping spherical particles. For a given normalized gray level (g_t) a Wiener filter is firstly applied to reduce the white noise component. Then the contour of the image is established. This is performed using a bilinear interpolation, achieving a subpixel resolution. The image is then binarized with threshold 0.5, making all pixels within the contour 1 and all outside 0. Working from this modified image, the diameter of the circle is computed.

Along the threshold contour the direction of the normal vector pointing outward is found and the gray level gradient along this vector at the boundary is interpolated and averaged over the entire contour circumference. However, according to Eq. (2), the sought gradient assumes a background level of zero (i.e., the background level is completely white), whereas in practice a non-zero background level exists. Thus, the computed gradient must be scaled with a factor related to the background gray level in the vicinity of the particle image. This adjusted gradient is then used with

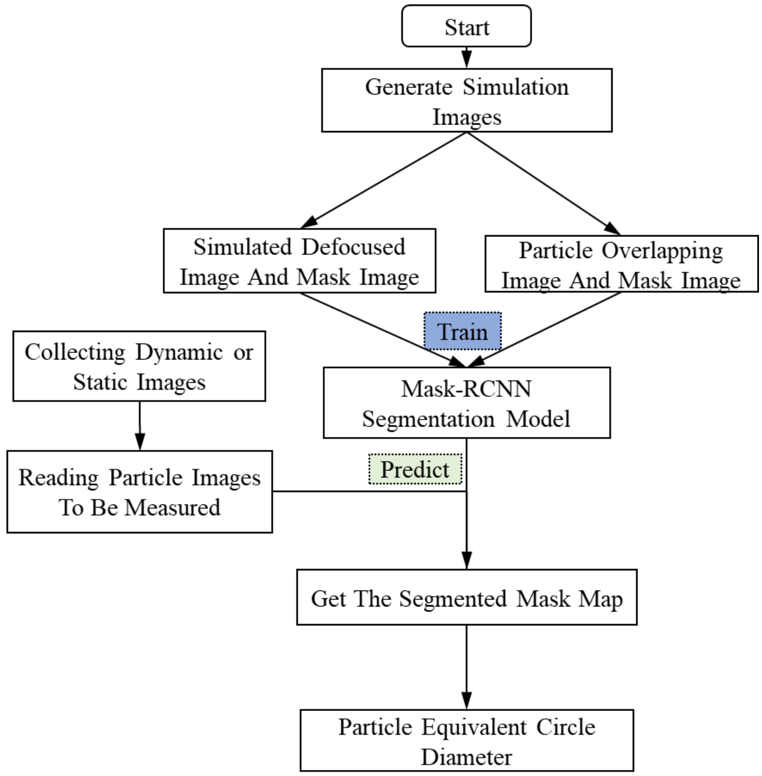

Figure 3. CNN based particle size and depth measurement process.

function f_2 to determine the blur kernel parameter $\tilde{\sigma}$ and further determine the size and position of a sphere in the object plane leading to this diameter on the image plane.

If now several spherical particles are in close proximity to one another, i.e., high number/volume concentration, then they will generate blurred images which are overlapping on the image plane. To analyse these images, the above algorithmic procedure is extended. First the contour of the overlapping particle images is determined at a selected g_t level, using a bilinear spline interpolation to achieve sub-pixel resolution. An ellipse is fitted to the g_t contour, determining a major and minor axis. Two criteria are then tested before proceeding. If the ratio of major to minor axis is less than 1.1, then the image is considered to be generated by a single particle and the standard procedure for analysing a single particle is invoked.

The second criterion is illustrated with Fig. 4, showing exemplary overlapping images of two neighbouring particles. The normalized gray level gradient around the circumference of the images is also shown. The two end points of the fitted ellipse are marked as points **a** and **e** in the image. Some smoothing of the gradient curve is performed before proceeding. First a representative value of the gray scale gradient at each end point is computed by averaging the gradient over the neighbouring 10 pixels. Then the gray level gradient is averaged over the portion of the g_t-contour, over which the values lie within $\pm 10\%$ of the representative value at the end points **a** and **e**. These portions of the contour used for averaging are marked on the graph of Fig. 4.

Once the two gray level gradient values and the associated blur kernel parameter $\tilde{\sigma}$ for each are determined, the diameter (or radius r_t) of each particle image at $g_\mathrm{t} = 0.5$ is computed, assuming circularity of the image and fitting (least squares) a circle to the portion of the g_t-contour used for the above gray level gradient averaging procedure. These two values of each particle, r_t and $\tilde{G}$, are then used to estimate the true sizes of the two particles, and using the calibration constant β, the z positions of the particles are found. Note that the calibration parameter β is the same for each particle, only the blur kernel parameter $\tilde{\sigma}$ may differ.

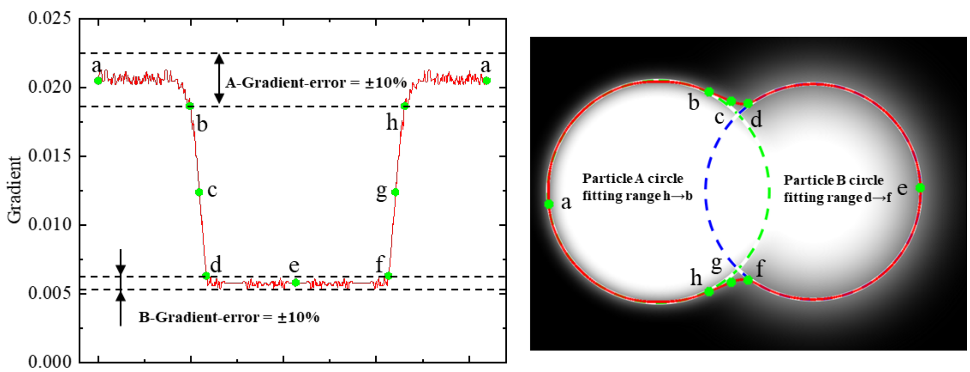

Figure 4. Normalized gray-level gradient computed from an image arising from two neighbouring particles with overlapping, blurred images. The two example particles have different z positions, but the same size.

Further discussion of the processing algorithm and subsequent validation requires some definition of overlap degree and for this the Overlap Ratio (OLR) has been introduced. The overlap ratio is pictorially depicted in Fig. 5 and is defined as $L/2R_\mathrm{B}$. R_B is the radius of Particle B and L is the distance the center of Particle B is offset from an initial distance $R_\mathrm{A} + R_\mathrm{B}$ toward the center of Particle A, with radius R_A. An overlap ratio of OLR≤ 0 indicates no overlap and an OLR > 1 designates complete overlap. Note, by definition, Particle B is always equal to or smaller in diameter than Particle A.

3.2. Generation of Synthetic Images

To simulate the intensity of a blurred image of a single spherical particle, $g_t(x, y)$, a simple convolution of the sharp image, $f(x, y)$, with a blur kernel , $h(x, y)$, suffices(Eq. (1)).

A modified procedure is followed to generate images arising from two or more particles in close proximity to one another such that their projected images overlap on the sensor plane. First the coordinates and sizes of the particles are prescribed, yielding two or more different values of σ according to the different Δz values (Eq. (4)). This results in different blur kernels, one for each of the particles. The subsequent procedure is graphically illustrated in Fig. 6.

First, the blurred image of the particle nearest to the backside illumination is generated, using a

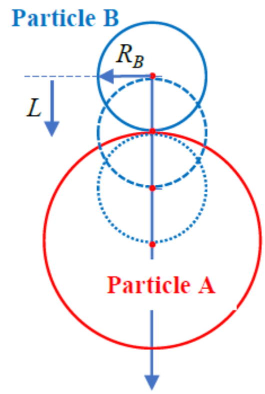

Figure 5. Sketch showing three different overlap degrees of particles **A** and **B**. The Overlap Ratio (OLR) is defined as $L/2R_{\mathrm{B}}$.

convolution of the normalized intensity image of the particle (Eq. (1)). This image is then inverted. Next, this inverted image is subtracted from the normalized image intensity of the particle nearer to the imaging side. This subtraction approximates the fact that the second particle is not entirely illuminated due to the shadowing effect of the first particle. The resulting image is then used as $f(x, y)$ in Eq. (1) to yield a blurred image. The final result of the overlapping images is then given by the inversion of the first blurred image minus the blurred image of the second particle. In principle, this procedure can be extended to more than two particles, always proceeding from the particles closest to the illumination side of the optical system.

The final image is adjusted to take into account the background illumination, denoted $b(x, y)$, i.e.,

$$g_{\mathrm{t}} = g_{\mathrm{t}} + b(x, y). \tag{10}$$

A background illumination is generally encountered in experiments, effectively altering the gray level gradient measured for a given blurred image. This is particularly important to consider when using conventional analysis, since the gray level gradient directly affects the position and size estimate. This background illumination can be estimated directly from the experimental images. For synthetic images, typical experimental values or a gray level with random fluctuations within a certain bit range of values can be used. Specific details of the background illumination used are given below in the respective sections.

4. Validation and Experiments

4.1. Experimental apparatus

To provide images from particles with known size, position, shape and degree of overlap, the apparatus schematically pictured in Fig. 7 was used. With this apparatus either one or two sample

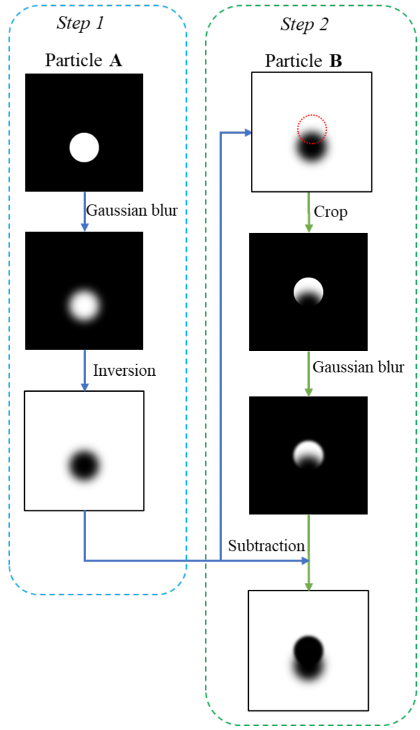

Figure 6. Graphical flowchart describing how the blurred image of multiple particles is generated.

plates can be mounted. The distance between the plates (δ) can be manually adjusted and the position of the plates can be traversed along the optical (z) axis using a stepper motor. Particles are placed on the plates before mounting. In this manner both in-focus and out-of-focus images of the same particles can be acquired. The in-focus images allow the exact shape and size of all particles on the respective sample plate to be determined. The origin of the z-axis is chosen such that $z = 0$ corresponds to the particle on plate **A** being in focus. The value of the manually adjusted δ is determined from the stepper motor displacement between the particles on the sample plates **A** and **B** being in focus. Thus, ground truth for both the particle size and position is always available to evaluate the accuracy of any DFD image processing algorithm.

To put the range of changes in z or δ expressed in millimeters into context, the depth of field for the optical system can be used for comparison. The depth of field is given approximately as

$$\mathrm{DOF} \approx 2cf^{\#}\left(\frac{z_0}{f} - 1\right) \tag{11}$$

where c is the circle of confusion, taken here as 0.03 mm, $f^{\#}$ is the f-stop (20.8), $f = 53$ mm is the focal length of the lens, and the standoff distance $z_0 = 86$ mm. This yields DOF ≈ 0.74 mm.

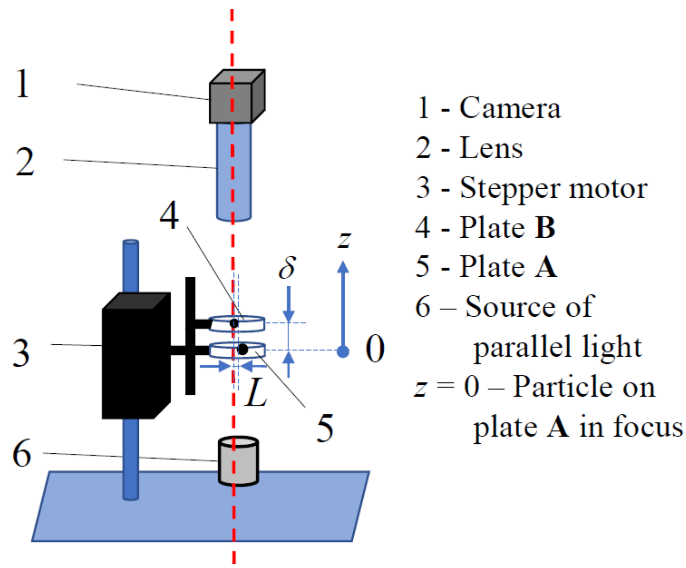

Figure 7. Schematic diagram of the experimental apparatus for generating images with known particle sizes, positions and shapes.

4.2. Validation of synthetic images

The validation of the image generation focuses on the validation of images generated for overlapping dual particles. There is no need to validate the generation of single particle blurred images, since the simulation uses an exact analytic expression. For images of dual overlapping particles, comparison can be made to laboratory results.

Before acquiring experimental images, reticles have been positioned at different z locations in the apparatus shown in Fig. 7, allowing the calibration factor β (Eq. (4)) to be determined. Hence, σ is known for each z position of the particle. These values of σ and the size of the particles were used for the synthetic generation of the blurred images.

In Figs. 8(a) and (b) a synthetic image of particles with overlapping blurred images is compared with a laboratory image. In Fig. 8(c) the gray scale profiles through the centerline of the two particle images are compared with one another, indicating excellent agreement.

4.3. Validation for particles with overlapping images

Validation of the analysis when overlapping images are acquired is performed using the apparatus described above in subsection 4.1 and using the images shown in Fig. 9. These images were generated by using calibration plates with varying dot sizes. Images were acquired for the three particle size combinations shown in Fig. 9 with varying OLR and with two values of δ, 0.1 mm and 0.4 mm. The intention of performing this systematic parameter variation is to provide a first qualitative impression of the maximum number concentration which can be reliably tolerated by

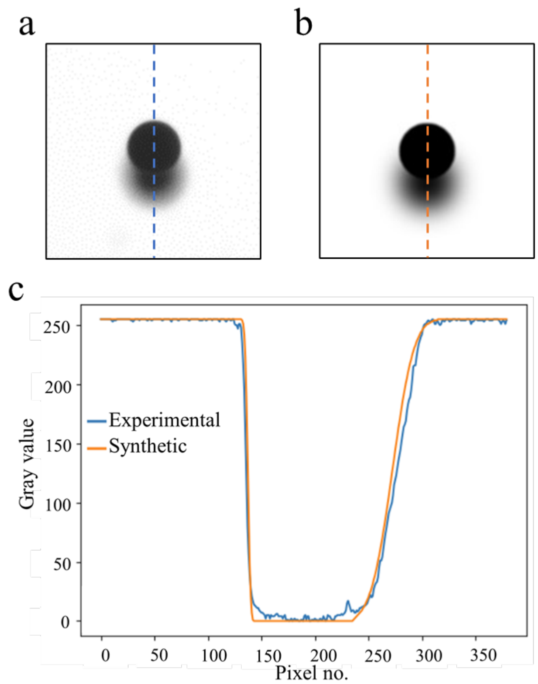

Figure 8. (a) Overlapping images obtained using the apparatus shown in Fig. 7; (b) Synthetic generation of two particles resulting in overlapping images. (c) Comparison of the gray level profiles through the centerline of the two images.

the DFD technique using this analysis algorithm. The results of this parametric study are shown in Fig. 10. In each of the four diagrams shown in this figure, the degree of blurring was systematically varied by changing z. For values of $z = 0$ Particle **A** is in focus and if $\delta = 0$, Particle **B** is also in focus. The validity limit of the processing algorithm, i.e., $\widetilde{\sigma} = 0.35$, is shown in each diagram as a vertical dashed line.

It is clear that in all cases of OLR = 0, the size evaluation is accurate up to the validity limit (and sometimes beyond). This is perhaps not intuitively obvious, since even with no overlap, the blur of each particle is mutually affecting the image of the other particle. However, the proposed algorithm eliminates these regions of mutual interaction when estimating $\tilde{\sigma}$. Furthermore, it appears that an overlap ratio of 0.4 appears to be tolerable, while still maintaining a size accuracy to within approx. 5%. Above this value of OLR, size measurements can still be performed, albeit only to within a lower range of $\tilde{\sigma}$ (degree of out-of-focus), especially for the smaller particle.

Restricting the OLR to 0.4 and below, the size estimate remains very accurate even with substantial values of δ, as indicated in Fig. 10d. Finally, it is instructive to compare the range over which reliable results can be achieved to the nominal DOF of the optical system (0.74 mm). For instance, for the 100 μm particle, a value of $\sigma/d_0 = \tilde{\sigma} = 0.35$ corresponds to approx. 2.95 mm, for the 200μm particle approx. 5.9 mm. This underlines how effective the DFD technique is in quantifying particle size far out of the depth of field.

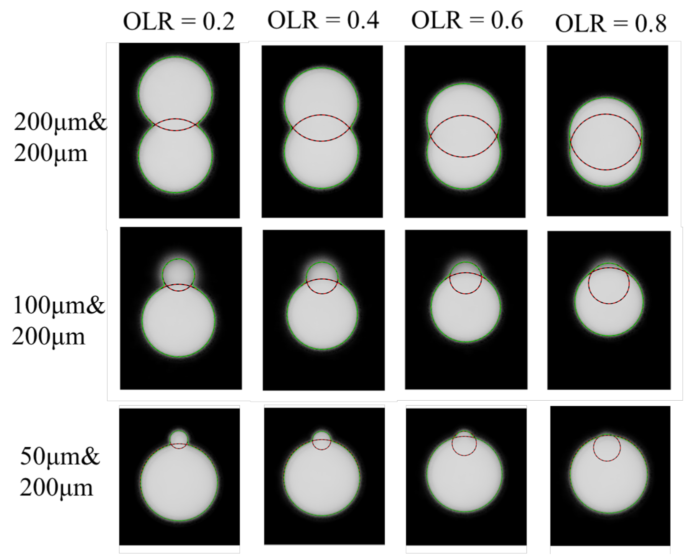

Figure 9. Example images with varying overlap ratios of two particles. Particle **A** has a diameter of 200 μm. Particle **B** varies in diameter between 50 μm and 200 μm. Example images for four overlap ratios are shown. The green circles give the contour at $g_{\mathrm{t}} = 0.5$ and the red circles are the circles fitted to the contour portion used for averaging the gray-level gradient. In these examples the particles have different z positions; hence different blur kernels.

Likewise, for testin the CNN algorithm, the same set of calibration plate images were used for verification. The images are first segmented according to the flow chart outlined in Fig. 3. Examples of the segmented images at varying values of particle size and OLR are shown in Fig. 11. The results of these validation tests are presented in Fig. 12, comparing results for different OLR, blur degrees, and the separation δ between two particles.

Examining the various graphs in Fig. 12, it is apparent that the CNN consistently delivers reliable results for single particle images up to the trained limit of $\tilde{\sigma} = 0.35$, irrespective of the particle size. In this respect, the CNN result is very similar to performance of the conventional processing using the theoretical solution as presented in Fig. 10, although exhibiting much less scatter with increase $\tilde{\sigma}$. At low overlapping ratios ($\mathrm{OLR} \leq 0.2$), the results continue to be very good, although sizing errors increase when the two particles are the same size (Fig. 12(c)). Interestingly, the measurement result is less sensitive to the particle separation (Fig. 12(d)). However, as the OLR increases, the performance decreases with the degree of out-of-focus, generally exhibiting an underestimation of the particle size (Fig. 12(a) and (b)). Nevertheless, the technique extends the particle sizing capability far beyond the conventional depth of focus limit, which in this case is 0.74 mm. To compare this limit to the normalized $\tilde{\sigma}$ shown on the graphs of Fig. 12, it is necessary to use Eq. (4), converting Δz into σ and then dividing by the particle diameter d_0. To do this, the parameter β for the system is required. In the present case, for the 200 μm particle, the limit $\tilde{\sigma} = 0.35$ corresponds to approx. 2.95 mm.

For purposes of evaluating the tolerable concentration limits now to be examined in section 5, the

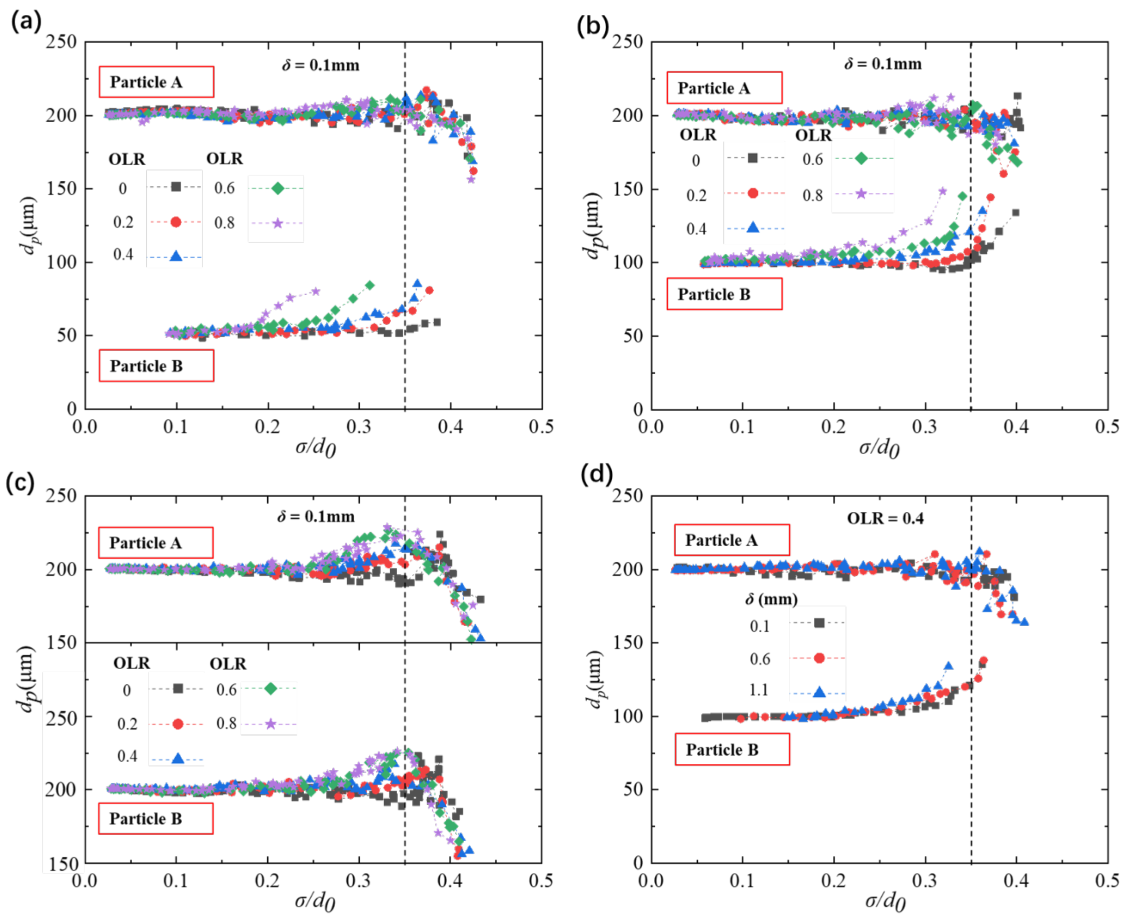

Figure 10. Parametric study in which the degree of blurring is varied by changing z. a), b) and c) uses a Particle **A** diameter of 200 μm, a $\delta = 0.1$ mm and a Particle **B** diameter of 50 μm, 100 μm and 200 μm respectively. d) The OLR is held constant at 0.4 and δ is varied using the particle diameter combination 100 μm and 200 μm. The vertical black dashed lines marked on the graphs indicate $\tilde{\sigma} = 0.35$, corresponding to the expected limitation of the single camera DFD technique.

results can be summarized as follows. Particles of all sizes with non-overlapping images can be reliably sized up to $\tilde{\sigma} = 0.35$. Particle pairs with an $\mathrm{OLR} \leq 0.2$ will also be sized correctly to within approx. $\pm 5\%$, and the separation of particles along the z axis does not degrade the size estimates significantly.

4.4. Example experiment

A second validation of the CNN image processing was performed using a rectangular channel flow seeded with polystyrene particles of diameter in the order of 100 μm. The flow system is schematically shown in Fig. 13, whereby the channel was constructed of transparent quartz glass with dimensions 10 mm (H) x 20 mm (W). The optical system, consisting of an illumination with

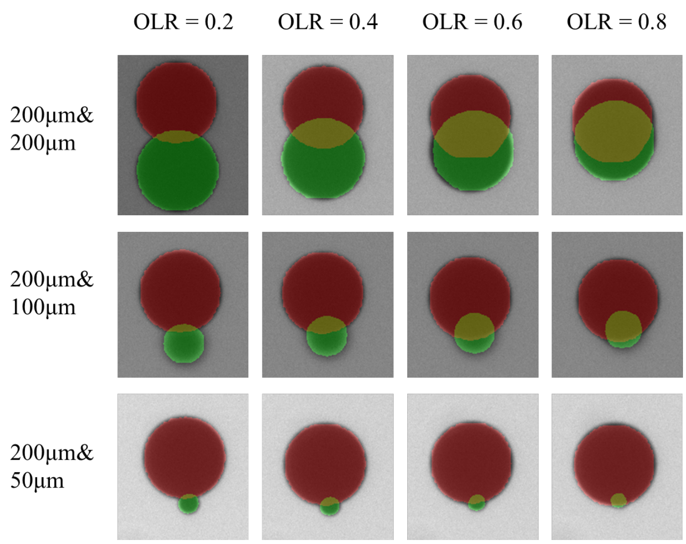

Figure 11. Example images with varying overlap ratios of two particles. Particle **A** has a diameter of 200 μm. Particle **B** varies in diameter between 50 μm and 200 μm. Example images for four overlap ratios are shown. The segmentation effects are represented by different colors in the figure.

parallel light, a lens and a camera, was so positioned such that the object plane was at the lower inner wall of the channel. The optical system had a depth of field of 0.74 mm.

In this experiment, there are two main steps. The first step involves capturing images of particles in a flowing state. A total of 3000 images are collected in this step, which are then processed using the CNN algorithm. The second step involves capturing images of particles in a stationary state. The procedure begins by turning on the circulation system to allow particles to flow, followed by stopping the flow and waiting for the particles to settle at the bottom of the channel before capturing an image. This process is repeated 300 times to collect focused images, serving as ground truth for the probability density distribution of size. These in-focus images were processed using a simple threshold method to determine their diameter.

In Fig. 14 and Tab. 1, the particle size probability density distribution measured with the flow on (blurred particle images) is compared with the distribution of the settled particles (in-focus particles). The particle size distributions based on the theoretical approach and CNN are both in very good agreement with ground truth.

Table 1. Measurement results of particle size of particles flowing in pipelines.

Algorithm	D_{10} μm	D_{50} μm	D_{90} μm
Ground Truth	95.4	100.3	107.8
DFD	94.7	100.6	108.3
CNN	92.5	99.8	116.5

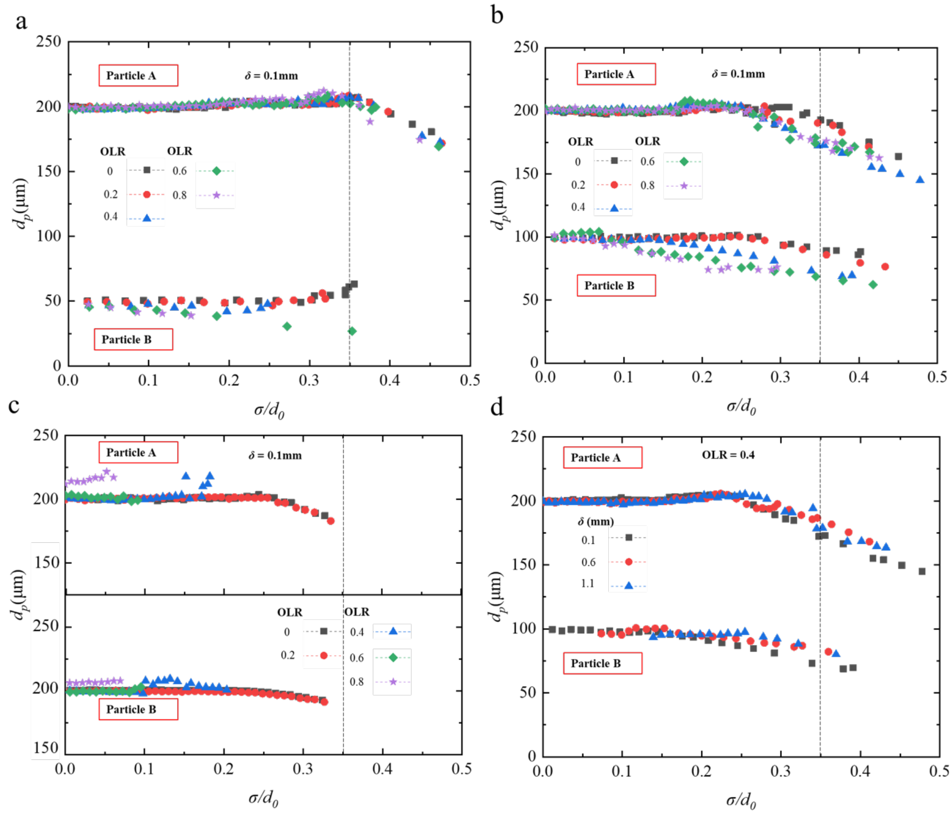

Figure 12. Parametric study in which the degree of blurring is varied by changing z. a), b) and c) uses a Particle **A** diameter of 200 μm, a $\delta = 0.1$ mm and a Particle **B** diameter of 50 μm, 100 μm and 200 μm respectively. d) The OLR is held constant at 0.4 and δ is varied using the particle diameter combination 100 μm and 200 μm.

5. Concentration limits

In the following section an attempt is made to quantify the tolerable limits of number/volume concentration which can be achieved using the DFD technique. This is a question which is of great practical significance, on the other hand there are numerous influencing parameters which make it difficult to deliver an estimate of universal validity. This difficulty will be elaborated by formulating a statement of the problem.

The situation to be studied is pictured in Fig. 15. A certain number of spherical particles are positioned randomly in a defined flow volume, shown in the figure as a black box. The embedded red box is the detection volume of the DFD system, the dashed line indicating the object plane. Note that, as described theoretically in Sharma et al. (2021), the depth of the detection volume will be particle size dependent, whereas the field of view is given by the magnification and sensor size. Hence, the number of overlapping blurred images and their degree of overlap (OLR) will depend on numerous factors: number of particles in the detection volume, size distribution of particles, location of the detection volume within the flow field. It is evident that a theoretical approach to

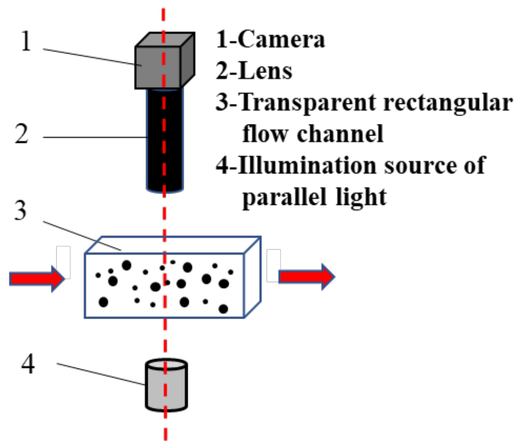

Figure 13. Schematic of experimental apparatus.

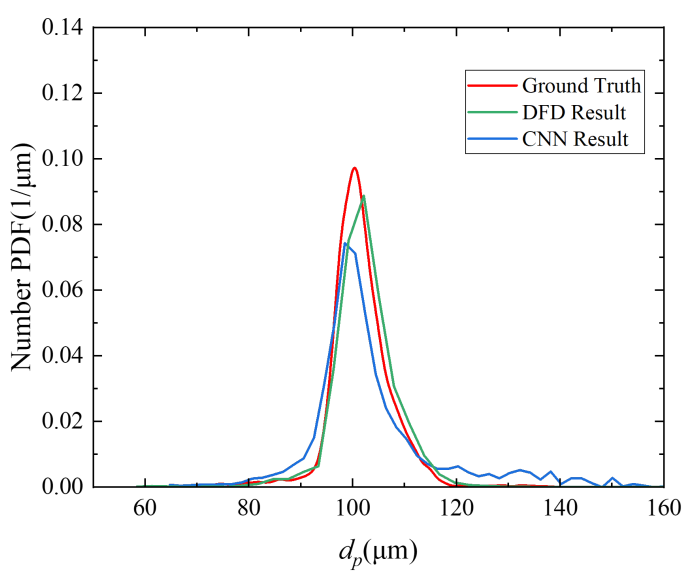

Figure 14. Comparison of particle size distribution obtained from in focus images (ground truth) and out-of-focus images using CNN processing.

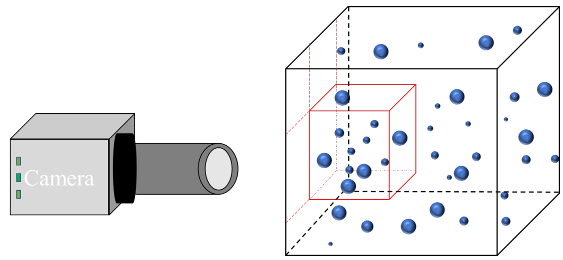

Figure 15. Pictorial rendition of high concentration particle generation: solid red box represents the volume of the imaging area, and black box represents the volume of the entire channel or flow field. The dashed plane represents the object plane of the DFD system.

estimating either the degree or the number of overlapping images would be extremely complex; therefore, in the present study this is investigated by simulating the system.

To begin this simulation, first a particle size distribution is prescribed. We have used a log-normal probability density function (PDF), given by

$$p(D) = \frac{1}{D\sigma_p\sqrt{2\pi}} \exp\left(-\frac{(\ln D - \mu)^2}{2\sigma_p^2}\right) \tag{12}$$

In this distribution the parameters μ and σ_p correspond to the expectation (mean) and the standard deviation respectively. The volume weighted mean particle diameter is given as the third moment of this distribution,

$$\begin{aligned} D_{30} &= \left(\int_0^\infty D^3 p(D)\mathrm{d}D\right)^{1/3} \\ &= e^{3(2\mu+3\sigma_p^2)/2} \end{aligned} \tag{13}$$

Note that the k^{th} moment of the log-normal distribution is given by $e^{k(2\mu+k\sigma_p^2)/2}$.

If now N particles are placed randomly in a volume V, the number concentration is simply $C_{\mathrm{N}} = N/V$ [#/m^3] and the volume concentration is $C_{\mathrm{V}} = N * D_{30}/V = V_{\mathrm{p}}/V$ [m^3/m^3]. The volume to be populated with particles will be defined by the field of view of the optical system (x,y) times the depth over which the largest particle can be detected. One must then position this detection volume in the larger outer volume (black box in Fig. 15). The blurred images of any particle behind or in front of the detection volume must also be added, since these images will contribute background noise to the images of particles within the detection volume. Some typical synthetic frames of defocussed particle images at various volume concentrations are shown in Fig. 16.

Figure 17 and Tab 2 shows the measured particle size distribution using the theoretical solution and the CNN algorithm for various volume concentrations, compared with the known ground truth. Even up to a volume concentration of 0.1% the distributions shows excellent agreement with the correct answer. It can be seen from the results that when the concentration is higher, the deviation

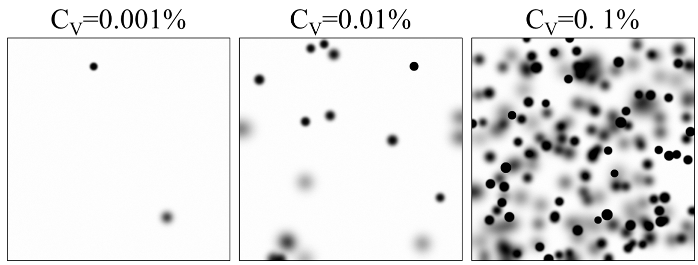

Figure 16. Synthetic camera frames of blurred particle images at different volume concentrations.

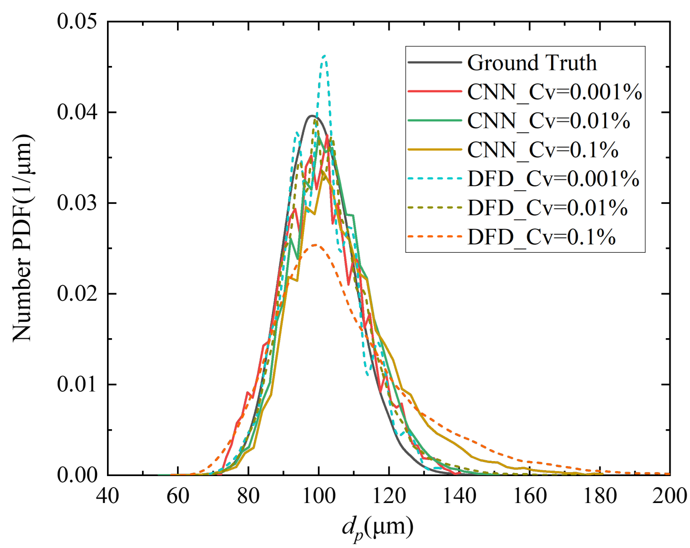

Figure 17. Measured particle size distribution from synthetic dataset at different volume concentrations.

Table 2. Particle size measurement results of simulated images with different volume concentrations.

C_v	Algorithm	D_{10} μm	D_{50} μm	D_{90} μm
	Ground Truth	87.25	99.24	113.18
0.001%	DFD	85.50	98.28	114.61
	CNN	84.80	98.64	114.88
0.01%	DFD	90.42	103.04	118.54
	CNN	88.23	101.78	115.37
0.1%	DFD	92.54	109.49	133.87
	CNN	89.20	103.55	125.81

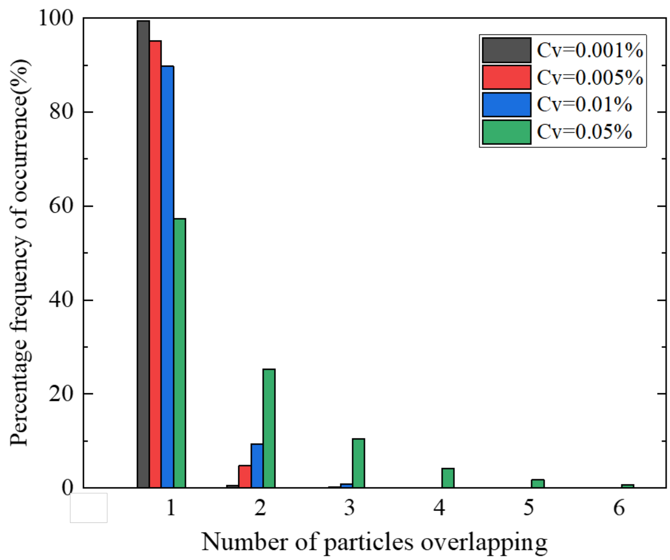

Figure 18. Percentage frequency at which the given number of particles overlap (line of sight). The summation of all bars of one colour equals 100.

measured by the DFD method is greater, but the particle size distribution is very consistent with the true value.

In Fig. 18 the relative occurrence of blurred images involving 1, 2 or more particles is plotted as a function of volume concentration. As an example, for a volume concentration of 0.01%, 90% of the images are of single particles, 9% involve two particles, and 1% involve three particles. Images with more than three particles are virtually non-existent. Given that the present CNN processing only handles single or dual particle images, this means that only 1% of the particles are not sized. On the other hand, there is no immediate grounds to infer that the size distribution will be biased by neglecting these 1% with multiple images overlapping.

Fig. 19 has been computed from the dataset generated to test the concentration limits of the DFD technique with the CNN processing. The log-normal particle size distribution used to generate this dataset has a mean of $\mu = ln(100)$ μm and a standard deviation of $\sigma_{\mathrm{p}} = 0.1$ μm. To continue with the above example, this distribution refers to the 9% with dual images overlapping. The probability of low overlap values is high, decreasing to almost zero at 100% overlap (OLR = 1). Only few particle pairs exhibit OLR> 1, which can only occur when a smaller particle overlaps with a larger particle.

6. Conclusions

In summary, this study presents two advancements in the Depth from Defocus (DFD) technique for characterizing dispersed two-phase flows. The first involves estimating the Gaussian blur kernel

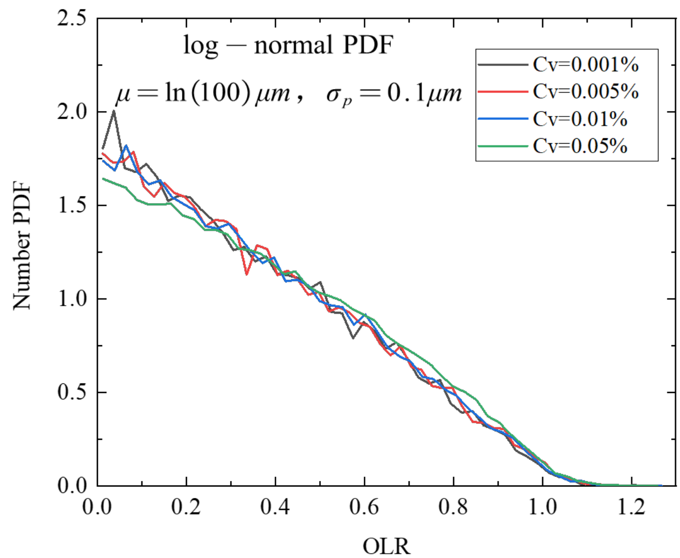

Figure 19. The frequency distribution of the overlapping of two particles with different volume concentrations.

from the average gray level gradient around the image contour. The second uses deep learning to identify defocused particles.

The first advancement addresses high number density dispersions where adjacent particle images overlap. We use a gradient based deblurring method to derive the blur kernel directly from the gray level gradient. Results show that for a blur kernel standard deviation of 0.35 and an overlap ratio (OLR) of 0.4, particle size measurement accuracy can reach ±5%. Although the overlap ratio limit cannot be directly converted to a number density limit, it serves as an important indicator of tolerable number densities. Position measurement accuracy is estimated at ±0.5 mm.

The second advancement introduces a method for generating synthetic blurred images for high number density particle images, which is validated using an experimental setup. This method allows for creating large datasets to train Mask R-CNN to identify and measure these images. The limitation of this method is defined by the dimensionless blur kernel size, $\tilde{\sigma} \leq 0.3$, meaning the degree of defocus should not exceed a standard deviation of 0.3 of the true particle diameter.

Simulation results reveal several insights. Even at high volume concentrations, the number of overlapping particle images remains moderate, with instances of three or more overlapping particles being rare. Most overlapping images have low OLR, ensuring high measurement accuracy even with significant defocus. Particle number concentration can also be reliably estimated with corrections for detection volume dependencies. This confirms that the DFD technique, combined with CNN processing, is a viable tool for studying dispersed two-phase flows. It offers high measurement accuracy across a wide range of particle sizes and can identify particle positions and number densities. This capability paves the way for three-dimensional velocity measurements using background illumination and a single camera.

Acknowledgements

This work was sponsored by the foundation of National Natural Science Foundation of China (No. 52376163) and National Foreign Expert Project (No. G2023013010) and the Shanghai Sailing Program (Grant No. 22YF1429600). The authors would like to gratefully thank Saini Jatin Rao from Indian Institute of Science Bangalore and Dr. Tianyi Cai from University of Shanghai for Science and Technology for extremely fruitful discussions.

References

Bao, X., & Li, M. (2011). Defocus and binocular vision based stereo particle pairing method for 3D particle tracking velocimetry. *Optics and Lasers in Engineering*, *49*(5), 623–631.

Barnkob, R., Cierpka, C., Chen, M., Sachs, S., Mäder, P., & Rossi, M. (2021). Defocus particle tracking: a comparison of methods based on model functions, cross-correlation, and neural networks. *Measurement Science and Technology*, *32*(9), 094011.

Barnkob, R., Kähler, C. J., & Rossi, M. (2015). General defocusing particle tracking. *Lab on a Chip*, *15*(17), 3556–3560.

Barnkob, R., & Rossi, M. (2020). General defocusing particle tracking: fundamentals and uncertainty assessment. *Experiments in Fluids*, *61*, 1–14.

Blaisot, J. B., & Yon, J. (2005, December). Droplet size and morphology characterization for dense sprays by image processing: application to the Diesel spray. *Experiments in Fluids*, *39*(6), 977–994. Retrieved from `http://link.springer.com/10.1007/s00348-005-0026-4` doi: 10.1007/s00348-005-0026-4

Cierpka, C., Segura, R., Hain, R., & Kähler, C. J. (2010). A simple single camera 3c3d velocity measurement technique without errors due to depth of correlation and spatial averaging for microfluidics. *Measurement Science and Technology*, *21*(4), 045401.

Dong, J., Roth, S., & Schiele, B. (2021). Dwdn: deep wiener deconvolution network for non-blind image deblurring. *IEEE Transactions on Pattern Analysis and Machine Intelligence*, *44*(12), 9960–9976.

Ens, J., & Lawrence, P. (1991). A matrix based method for determining depth from focus. In *Proceedings. 1991 ieee computer society conference on computer vision and pattern recognition* (pp. 600–601).

Jatin Rao, S., Sharma, S., Basu, S., & Tropea, C. (2024). Depth from defocus technique: A simple calibration-free approach for dispersion size measurement. *Experiments in Fluids (accepted for publication Feb. 2024)*.

Junjie, T., Yinghui, W., Haomiao, M., Tao, Y., Lingyu, A., ZHANG, S., & Wei, L. (2023). An image defocus deblurring method based on gradient difference of boundary neighborhood. *Virtual Reality & Intelligent Hardware*, *5*(6), 538–549.

Lebrun, D., Ozkul, C., Touil, C., Blaisot, J., & Kleitz, A. (1994). Simultaneous particle size, 3d position and velocity measurements from processing of defocused images recorded with two ccd cameras. In *Optical measurements and sensors for the process industries* (Vol. 2248, pp. 294–306).

Levin, A., Fergus, R., Durand, F., & Freeman, W. T. (2007). Image and depth from a conventional camera with a coded aperture. *ACM Transactions on Graphics (TOG)*, *26*(3), 70–es.

Lin, T.-Y., Maire, M., Belongie, S., Hays, J., Perona, P., Ramanan, D., … Zitnick, C. L. (2014). Microsoft coco: Common objects in context. In *Computer vision–eccv 2014: 13th european conference, zurich, switzerland, september 6-12, 2014, proceedings, part v 13* (pp. 740–755).

Murata, S., & Kawamura, M. (1999). Particle depth measurement based on depth-from-defocus. *Optics & Laser Technology*, *31*(1), 95–102.

Pentland, A. P. (1987). A new sense for depth of field. *IEEE Transactions on Pattern Analysis and Machine Intelligence*(4), 523–531.

Pereira, F., & Gharib, M. (2002). Defocusing digital particle image velocimetry and the three-dimensional characterization of two-phase flows. *Measurement Science and Technology*, *13*(5), 683.

Rao, S. J., Sharma, S., Basu, S., & Tropea, C. (2024). Depth from defocus technique: a simple calibration-free approach for dispersion size measurement. *Experiments in Fluids*, *65*(4), 1–22.

Rao, S. J., Sharma, S., Tropea, C., & Basu, S. (2024). *A method and apparatus for measuring geometric characteristics of particles.* (Indian Patent 518811)

Ratz, M., Sachs, S., König, J., & Cierpka, C. (2023). A deep neural network architecture for reliable 3d position and size determination for lagrangian particle tracking using a single camera. *Measurement Science and Technology*, *34*(10), 105203.

Richardson, W. H. (1972). Bayesian-based iterative method of image restoration. *JoSA*, *62*(1), 55–59.

Sachs, S., Ratz, M., Mäder, P., König, J., & Cierpka, C. (2023). Particle detection and size recognition based on defocused particle images: a comparison of a deterministic algorithm and a deep neural network. *Experiments in Fluids*, *64*(2), 21.

Sharma, S., Rao, S. J., Chandra, N. K., Kumar, A., Basu, S., & Tropea, C. (2023). Depth from defocus technique applied to unsteady shock-drop secondary atomization. *Experiments in Fluids*, *64*(4), 65.

Sharma, S., Singh, A. P., Rao, S. S., Kumar, A., & Basu, S. (2021). Shock induced aerobreakup of a droplet. *Journal of Fluid Mechanics*, *929*.

Subbarao, M. (1988). Parallel depth recovery by changing camera parameters. In *Iccv* (pp. 149–155).

Subbarao, M., & Gurumoorthy, N. (1988). Depth recovery from blurred edges. In *Proceedings cvpr'88: The computer society conference on computer vision and pattern recognition* (pp. 498–499).

Surya, G., & Subbarao, M. (1993). Depth from defocus by changing camera aperture: A spatial domain approach. In *Proceedings of ieee conference on computer vision and pattern recognition* (pp. 61–67).

Wang, Z., He, F., Zhang, H., Hao, P., Zhang, X., & Li, X. (2022a). Characterization of the in-focus droplets in shadowgraphy systems via deep learning-based image processing method. *Physics of Fluids*, *34*(11).

Wang, Z., He, F., Zhang, H., Hao, P., Zhang, X., & Li, X. (2022b). Three-dimensional measurement of the droplets out of focus in shadowgraphy systems via deep learning-based image-processing method. *Physics of Fluids*, *34*(7).

Wiener, N. (1949). *Extrapolation, interpolation, and smoothing of stationary time series: with engineering applications*. The MIT press.

Willert, C., & Gharib, M. (1992). Three-dimensional particle imaging with a single camera. *Experiments in Fluids*, *12*, 353–358.

Xu, R., Huang, Z., Gong, W., Zhou, W., & Tropea, C. (2024). Depth from defocus technique for high number densities and non-spherical particles. *Measurement, revision being reviewed*.

Zhang, X., Dong, Z., Wang, H., Sha, X., Wang, W., Su, X., … Yang, S. (2023). 3d positioning and autofocus of the particle field based on the depth-from-defocus method and the deep networks. *Machine Learning: Science and Technology*.

Zhou, W., Luo, X., Chen, B., Zhang, Y., & Cai, X. (2020). Estimation of particle depth from two defocused images using the Fourier transform. *Particuology*, *49*, 48–54.

Zhou, W., Tropea, C., Chen, B., Zhang, Y., Luo, X., & Cai, X. (2020). Spray drop measurements using depth from defocus. *Measurement Science and Technology*, *31*(7), 075901.

Zhou, W., Zhang, Y., Chen, B., Tropea, C., Xu, R., & Cai, X. (2021). Sensitivity analysis and measurement uncertainties of a two-camera depth from defocus imaging system. *Experiments in Fluids*, *62*(11), 1–14.